Communication

Revealing the Subsurface Basal ⟨a⟩ Dislocation Activity in Magnesium Through Lattice Rotation Analysis

BIJIN ZHOU, LEYUN WANG, WENJUN LIU, XIAOQIN ZENG, and YANJUN LI

A method was proposed in this study to reveal the subsurface basal dislocation activity in Mg-Y alloy and determine the corresponding Burgers vector. This is achieved by correlating the slip directions of dislocations to the lattice rotation represented by the {0001} pole figure. The identified basal slip system by this approach was verified by micro-Laue diffraction. This method can be applied as a complementary method to the conventional slip trace analysis to study the dislocation behavior of Mg alloys.

It is generally believed that basal ⟨a⟩ dislocation slip dominates the deformation of polycrystalline magnesium (Mg) alloys at room temperature as the critical resolved shear stress (CRSS) for basal ⟨a⟩ dislocation slip is considerably lower than that for non-basal dislocation slip.[1–4] The activation of basal ⟨a⟩ dislocations in Mg alloys can also trigger other important cross-grain boundary deformation mechanisms like slip transfer,[5] slip-induced twinning,[6] and twin boundary migration.[7] To understand these triggered deformation modes, precise identification of the basal ⟨a⟩ dislocation type is important.

Dislocation behavior in Mg alloys can be studied by surface slip trace analysis.[8–12] The activated slip systems in each grain can be identified by the observed slip traces (i.e., intersection of the slip plane and the sample surface) when the grain orientation has been measured by electron back scatter diffraction (EBSD).[8–18] A limitation of the EBSD-based slip trace analysis is that it cannot determine the Burgers vector of the activated basal ⟨a⟩ dislocations because three possible basal ⟨a⟩ slip systems possess the same surface slip trace.[11,16,17] Recently, a method to determine the Burgers vectors of basal ⟨a⟩ dislocations was proposed by Xu et al.,[16] where a combination of grain orientation mapping by EBSD and high-resolution digital image correlation (HRDIC) analysis of shear strain was used. Their method relied on visible surface slip traces and powerful data post-processing. However, when basal slip traces are invisible, such as in the circumstance that the corresponding Burgers vectors are almost parallel to the surface with little out-of-plane component, it seems impossible to identify basal slip systems by surface slip trace analysis or Xu's method.[16] This situation is actually very common in the as-rolled or as-extruded Mg alloys,[9,11–13,15] in which the basal plane of most grains is parallel to the rolling direction or the extrusion direction; samples extracted from Mg-rolled sheets and extruded bars often have their surface being parallel to the basal plane of most grains. Even if basal ⟨a⟩ dislocations are activated in many grains, basal slip traces are hardly observed. For instance, Boehlert et al. studied a rolled AZ31 (Mg-3Al-1Zn, wt pct) alloy based on surface slip trace analysis and reported more than 50 pct deformed grains did not exhibit any surface slip traces.[11] To characterize subsurface basal ⟨a⟩ dislocation activity, it is important to develop an analysis method.

In the present work, we report an experimental method to reveal the subsurface basal ⟨a⟩ dislocation activity in Mg and identify the type of the subsurface basal ⟨a⟩ dislocation based on the lattice rotation analysis using EBSD data. The validity of this method was confirmed via micro-Laue diffraction.

The material used in this study was an extruded Mg-5Y (wt pct) alloy with an average grain size of 96 μm. The processing history (casting and extrusion) of this material has been reported in Reference 19. A tensile sample with nominal gauge dimensions of 18.0 mm × 3.4 mm × 1.4 mm (Length × Width × Thickness) was fabricated by electron discharge machining, with the tensile direction (TD) being parallel to the extrusion direction (ED). The top surface of the sample was ground, polished, and chemo-mechanical-polished in Oxide Polishing Suspension (OPS). Afterwards, the sample was tensioned by a Zwick/Roell Z020 testing machine with initial strain rate of 4.6×10^{-4} s^{-1}. When

BIJIN ZHOU is with the National Engineering Research Center of Light Alloy Net Forming, Shanghai Jiao Tong University, Shanghai 200240, P.R. China and also with the Department of Materials Science and Engineering, Norwegian University of Science and Engineering, 7491 Trondheim, Norway. LEYUN WANG is with the National Engineering Research Center of Light Alloy Net Forming, Shanghai Jiao Tong University. Contact e-mail: leyunwang@sjtu.edu.cn WENJUN LIU is with the Advanced Photon Source, Argonne National Laboratory, Argonne, IL 60439. XIAOQIN ZENG is with the National Engineering Research Center of Light Alloy Net Forming, Shanghai Jiao Tong University and also with the State Key Laboratory of Metal Matrix Composites, Shanghai Jiao Tong University, Shanghai 200240, P.R. China. Contact e-mail: xqzeng@sjtu.edu.cn YANJUN LI is with the Department of Materials Science and Engineering, Norwegian University of Science and Technology. Contact e-mail: yanjun.li@ntnu.no
Manuscript submitted April 22, 2020.
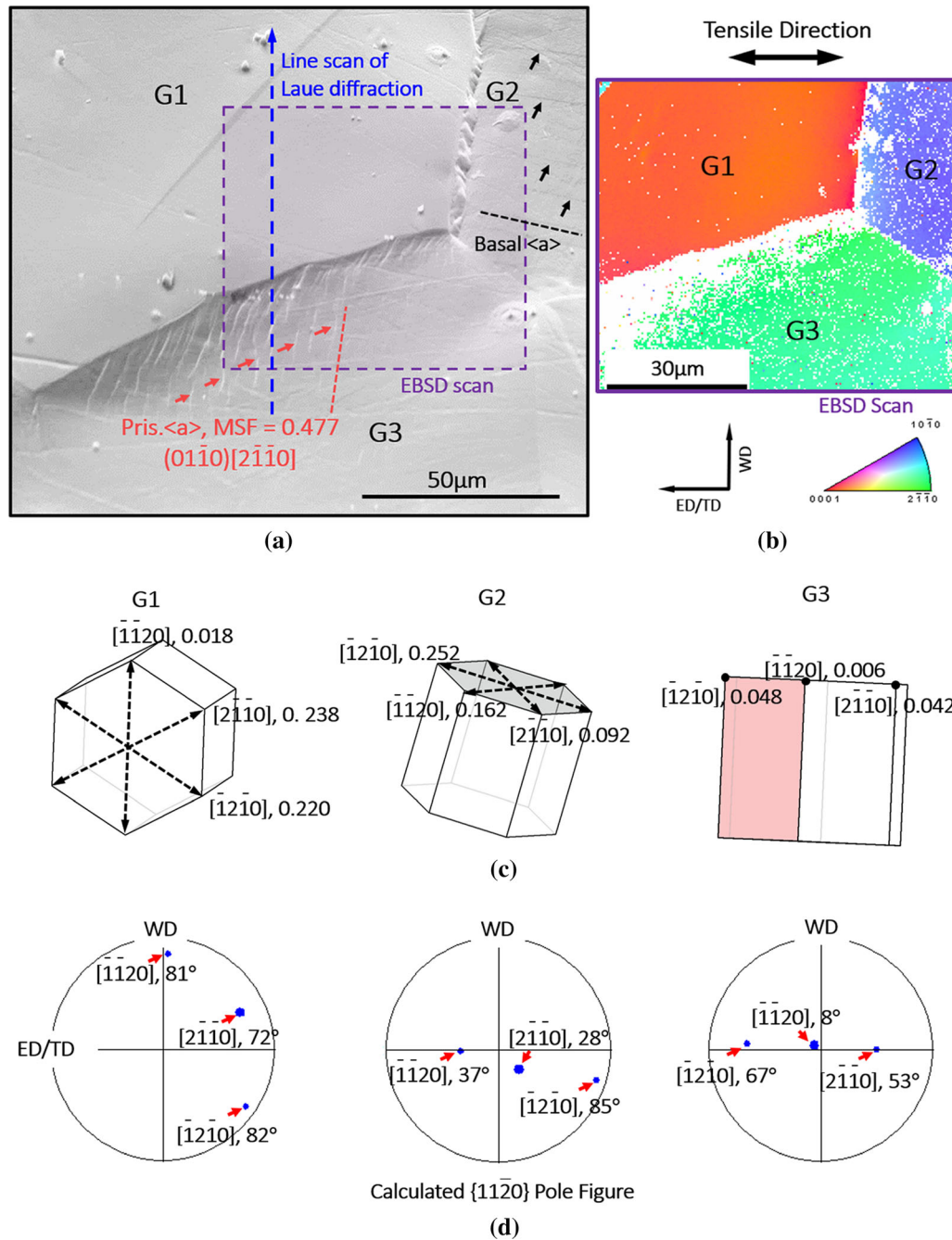Article published online July 10, 2020.

Fig. 1—Microstructure of the region of interest and evaluation for the visibility of basal slip traces in the studied grains. (*a*) SEM image of the region of interest. (*b*) EBSD inverse pole figure (IPF) map providing orientation information of G1, G2, and G3, with average Euler angles (207, 18, 88 deg), (254, 104, 65 deg), and (267, 86, 37 deg), respectively. (*c*) Hexagonal unit cells of G1–G3 projected on the ED/TD–WD plane. The basal slip systems were indexed, and the corresponding macro Schmid factors (MSFs) were listed as well. G3 has an orientation favoring the activation of prismatic ⟨a⟩ slip system (the red plane, $(01\bar{1}0)[2\bar{1}\bar{1}0]$, MFS = 0.477). (*d*) Calculated $11\bar{2}0$ pole figures of the three grains, which give the angles between the slip directions (Burgers vectors) and the sample surface normal. Evaluation for the visibility of basal slip traces is based on these calculated angles: the larger an angle is, the less possibility the corresponding slip trace can emerge on the sample surface.

the engineering strain reached 4.5 pct, the sample was unloaded and then scanning electron microscope (SEM, FEI, NOVA NanoSEM 230) was used to image a region of interest in the deformed sample. Orientation data were obtained subsequently by EBSD mapping using operating voltage of 20 kV, step size of 0.4 μm, and spot size of 6. The working distance and sample tilt are 13 mm and 70 deg, respectively.

The micro-Laue diffraction experiment was conducted at the beamline 34-ID-E of the Advanced Photon Source (APS) in the Argonne National Laboratory. A polychromatic X-ray microbeam with a beam size of ~

$0.5 \times 0.5\ \mu m^2$ was used to scan a $100\ \mu m$ length on the surface of the deformed sample to obtain a *subsurface* 2D microstructure map. The sample's ED/TD was oriented at a 45 deg angle to the incoming X-ray and the CCD area detector, which was located approximately 510 mm above the sample to collect Laue diffraction patterns. A data package of the diffraction patterns was obtained by differential aperture X-ray microscopy (DAXM).[20] The methodology to build a correlation between dislocation types and stretched Laue diffraction peaks can be found in References 21 through 23. We used a MATLAB^{TM} script to simulate the streak directions of the collected Laue diffraction peaks. By comparing the streak directions of the experimental Laue diffraction peaks and the simulated streak directions, the type of dislocations in a detected voxel can be identified.

Figure 1(a) shows the location of the line scan of Laue diffraction and three neighboring grains labeled as G1, G2, and G3. The inverse pole figure (IPF) map of the box region in Figure 1(a) is shown in Figure 1(b). As can be seen, there are slip traces in G2 and G3. The slip traces in G2 pointed out by black arrows have a good alignment with basal plane. Non-basal slip traces are observed in G3: the slip traces pointed out by red arrows have a good alignment with prismatic $(01\bar{1}0)$ plane. The corresponding prismatic slip system $(01\bar{1}0)[2\bar{1}\bar{1}0]$ has a macro Schmid factor (MSF) up to 0.477. Figure 1(c)

shows the hexagonal unit cell of each grain. All the possible basal slip systems with the corresponding MSFs were listed as well. G1 and G2 have two and one basal slip systems with MSFs lager than 0.2, respectively. However, all the basal slip systems in G3 have near-zero MSFs. This is consistent with non-basal dislocation activities observed in Figure 1(a). Figure 1(d) provides the angles between the basal $\langle a \rangle$ slip directions and the normal of the ED/TD–WD plane to reflect the visibility of basal slip traces in the grains under SEM. Within G1, the basal slip systems $(0001)[2\bar{1}\bar{1}0]$ (MSF = 0.238) and $(0001)[\bar{1}2\bar{1}0]$ (MSF = 0.220), with the large angles between the Burgers vectors and the sample surface normal (72 and 82 deg, respectively), have the possibilities to be activated, but the corresponding slip traces are *invisible* on the sample surface.

To reveal the dislocation activity in G1, its orientation has been closely examined. Figure 2(a) shows the misorientation distribution map of G1. A clear band-shaped zone with distinct misorientation from the rest of the grain can be observed. A misorientation profile across the band is shown in Figure 2(b). A long-range misorientation gradient can be clearly seen, indicating that dislocation slip is activated in G1 and preserved as geometrically necessary dislocations (GNDs). Figure 2(c) depicts the $\{0001\}$ and $\{11\bar{2}0\}$ pole figures for the box region in Figure 2(a). An enlarged portion of the $\{0001\}$ pole figure shows that there is an obvious
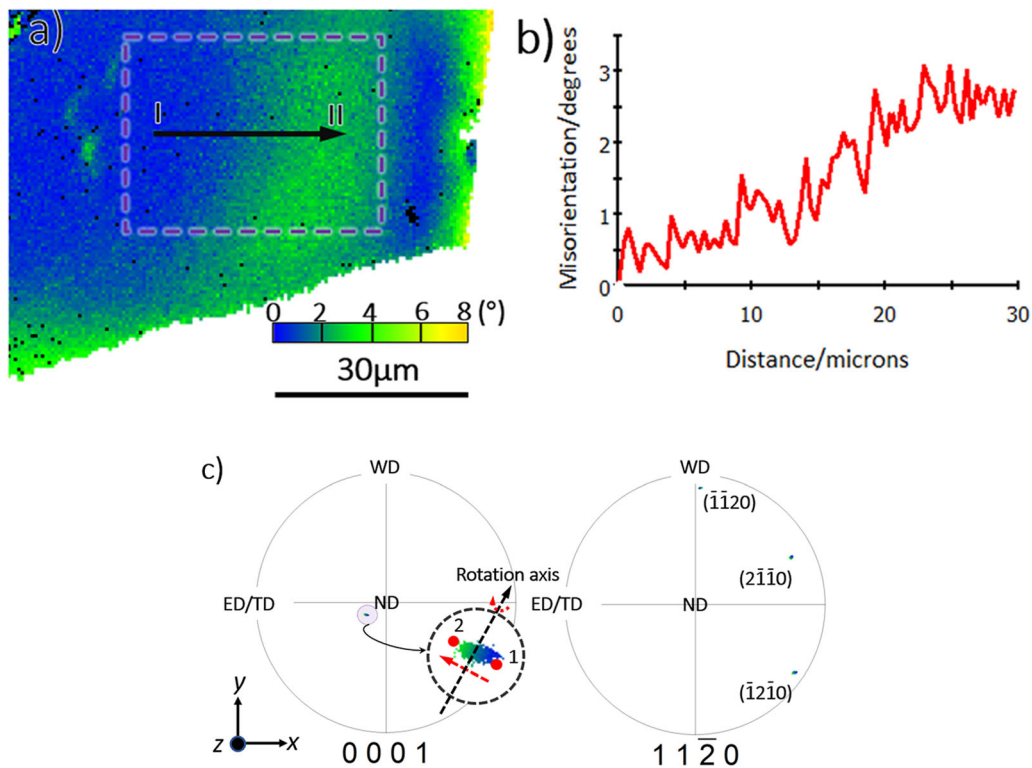

Fig. 2—Misorientation gradient of G1 presented in different dimensions. (*a*) Misorientation distribution map of G1 inside which a clear band-shaped misorientation gradient exists. (*b*) Misorientation profile along the horizontal arrow in (a). (*c*) {0001} and {11$\bar{2}$0} pole figures of the area encircled by the box in (b) where the (0001) pole is stretched nearly along the direction from the center of the {11$\bar{2}$0} pole figure to the ($\bar{1}2\bar{1}0$)pole.
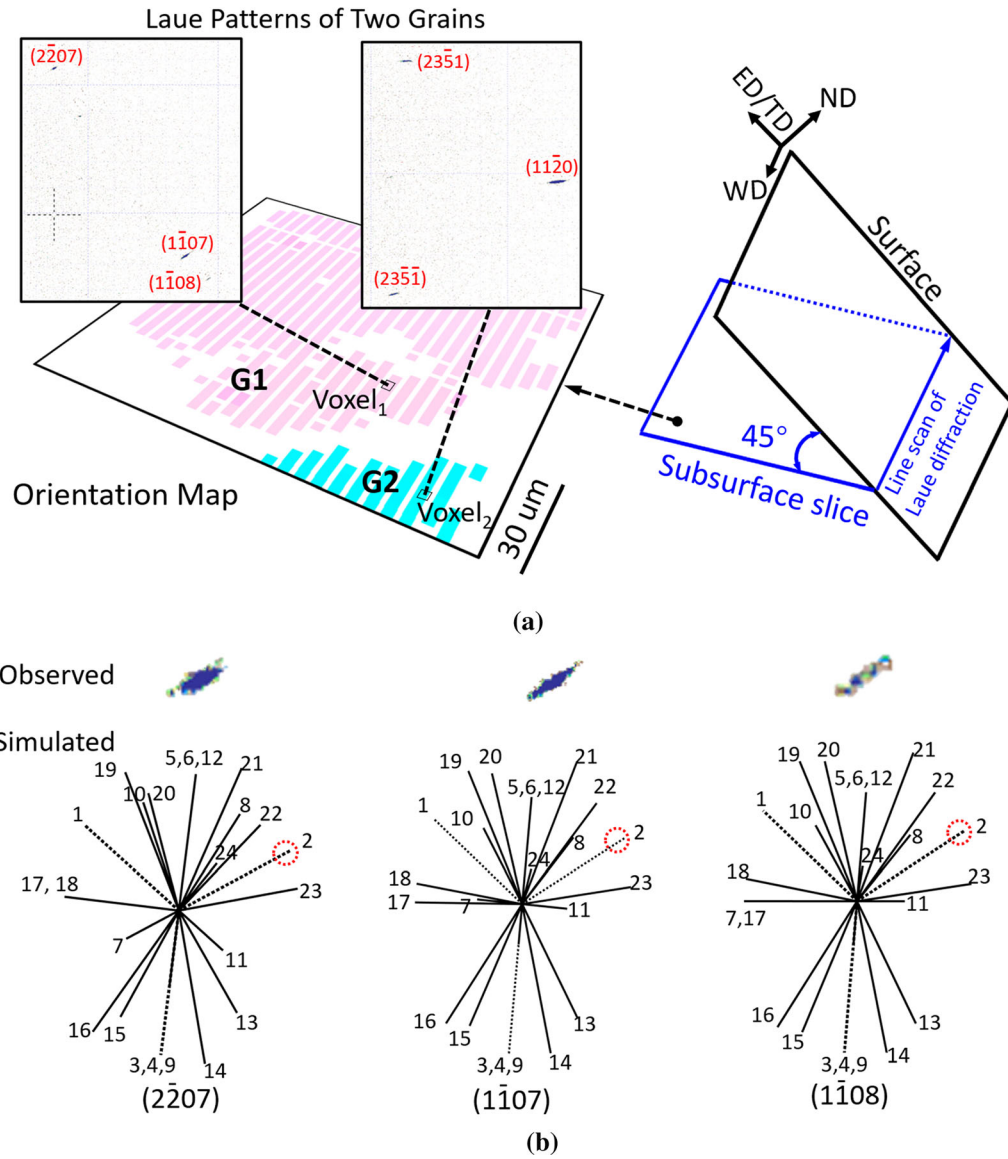
Fig. 3—Laue-diffraction-based GND-type analysis. (*a*) Subsurface orientation map of G1 and G2. (*b*) Simulated streak directions corresponding to the three peaks with the assumption of GNDs from 24 possible slip systems. Slip system #2 $(0001)[1\bar{2}\bar{1}0]$ provides the best match between the simulated and the observed streak directions of the Laue diffraction peaks.

stretching of (0001) pole (see the red arrow from the point 1 to 2), which represents a lattice rotation of G1. The two-dimension (2D) coordinates of point 1 is $(-0.133, -0.105)$; the 2D coordinates of point 2 is $(-0.173, -0.085)$. By the transfer formula from 2D (X, Y) to 3D coordinates $(x, y, z) = \left(\frac{2X}{1+X^2+Y^2}, \frac{2Y}{1+X^2+Y^2}, \frac{1-X^2-Y^2}{1+X^2+Y^2}\right)$, the space vectors of points 1 and 2 in Figure 2(c) were calculated as $\boldsymbol{n_1}$ $(-0.258, -0.204, 0.944)$ and $\boldsymbol{n_2}$ $(-0.333, -0.164, 0.929)$ according to the x (-ED/-TD)—y (WD)—z (ND) coordinate system (right-handed Cartesian coordinate system), respectively. The rotation axis $(\boldsymbol{n_1} \times \boldsymbol{n_2})$ can be calculated as $(0.402, 0.866, 0.297)$, which is very close to the space vector of $[10\bar{1}0]$: $(0.523, 0.809, 0.256)$. The angle between $[10\bar{1}0]$ and the calculated rotation axis $(\boldsymbol{n_1} \times \boldsymbol{n_2})$

is 9 deg, which implies that the lattice of G1 may have rotated around $[10\bar{1}0]$ axis. It is well known that basal $\langle a \rangle$ dislocation activities will cause lattice rotation around $\langle 10\bar{1}0 \rangle$ axes where each rotation axis is perpendicular to both the corresponding Burgers vector and basal plane normal.[24–26] Thus, the local deformation in G1 is suspected to be caused by the basal $\langle a \rangle$ dislocation activity.

The space vectors of basal $\langle a \rangle$ slip direction $[\bar{1}\bar{1}20]$, $[2\bar{1}\bar{1}0]$, and $[\bar{1}2\bar{1}0]$ of G1 are calculated as $\boldsymbol{b_1}$ $(0.050, 0.984, 0.170)$, $\boldsymbol{b_2}$ $(0.867, 0.417, 0.273)$, and $\boldsymbol{b_3}$ $(0.833, -0.547, -0.069)$, respectively. To examine which basal slip system has caused the lattice rotation of G1, the angles between the rotation axis $(\boldsymbol{n_1} \times \boldsymbol{n_2})$ and the three Burgers vectors $(\boldsymbol{b_1}, \boldsymbol{b_2},$ and $\boldsymbol{b_3})$ are calculated. The results are $\boldsymbol{b_1}\hat{}(\boldsymbol{n_1} \times \boldsymbol{n_2}) = 22$ deg, $\boldsymbol{b_2}\hat{}(\boldsymbol{n_1} \times \boldsymbol{n_2}) = 38$ deg,

and $\mathbf{b_3}\hat{}(\mathbf{n_1} \times \mathbf{n_2})$ = 81 deg, showing that the Burgers vector $[\bar{1}2\bar{1}0](\mathbf{b_3})$ is almost perpendicular to the rotation axis $\mathbf{n_1} \times \mathbf{n_2}$. Note that the hexagonal lattice was considered during the whole analysis process. It confirms that the rotation of (0001) pole in Figure 2(c) is caused by the activity of the basal slip system with Burgers vector $[\bar{1}2\bar{1}0]$ (MSF = 0.220, #2 ranked) instead of Burgers vector $[2\bar{1}\bar{1}0]$ (MSF = 0.238, #1 ranked) in G1. This "non-Schmid" activation can also be reflected by Figure 2(c) where the (0001) pole (*i.e.*, the normal vector of the basal plane of G1) has gradually moved away from ND, instead of moving towards ND in the pole figure according to the macro tensile strain.[27] Although this finding is not very surprising as the micro stress status of grains does not always follow the macro stress, it emphasizes that the activated basal slip system cannot be identified solely by the macro Schmid criterion.[16]

To verify the identified basal ⟨a⟩ dislocation slip in G1, micro-Laue diffraction was used to map the *subsurface* microstructure. Figure 3(a) shows an orientation map that was extracted from the line scan of Laue diffraction marked in Figure 1(a) as well as two sample Laue patterns from G1 and G2, respectively. As can be seen in the two Laue patterns, the indexed diffraction peaks are stretched, confirming the existence of GNDs.[28,29] The slip systems of the GNDs can be inferred from the streak directions of the diffraction peaks. Figure 3(b) shows an example to identify the GND type in the voxel of G1. The theoretical streak directions for $(2\bar{2}07)$, $(1\bar{1}07)$, and $(1\bar{1}08)$ diffraction peaks in G1 were simulated for 24 slip systems (basal slip $\{0001\}\langle11\bar{2}0\rangle$:1 to 3, prismatic slip $\{1\bar{1}00\}\langle11\bar{2}0\rangle$: 4 to 6, pyramidal ⟨a⟩ slip $\{1\bar{1}01\}\langle11\bar{2}0\rangle$: 7 to 12, and pyramidal ⟨c+a⟩ slip $\{1\bar{1}01\}\langle2\bar{1}\bar{1}3\rangle$: 13 to 24) in Mg. The simulated streak directions associated with slip system #2 $(0001)[\bar{1}2\bar{1}0]$ matches the observed streak directions for all the three peaks. This indicates that the voxel contains GNDs of basal slip system $(0001)[\bar{1}2\bar{1}0]$, which is the same as the type that identified by the

EBSD analysis method based on lattice rotation mechanism.

The above peak streak analysis was performed for *all* voxels in G1 and G2, and the identified dislocation slip systems are shown in Figure 4 where voxels are colored according to the GND types: light blue for basal ⟨a⟩ slip $(0001)[\bar{1}2\bar{1}0]$, purple for pyramidal ⟨a⟩ slip $(\bar{1}011)[\bar{1}2\bar{1}0]$, deep blue for pyramidal ⟨c+a⟩ slip $(1\bar{1}01)[\bar{1}2\bar{1}3]$, green for pyramidal ⟨c+a⟩ slip $(\bar{1}101)[\bar{1}2\bar{1}3]$, red for prismatic ⟨a⟩ slip $(01\bar{1}0)[2\bar{1}\bar{1}0]$, and orange for pyramidal ⟨a⟩ slip $(01\bar{1}1)[2\bar{1}\bar{1}0]$. Their MSFs are listed in Figure 4 as well. Note that if a voxel has diffraction peaks without apparent stretching, it is colored in gray. The GND distribution map obtained by Laue diffraction indicates that there is a large fraction of basal ⟨a⟩ dislocations with Burgers vector $[\bar{1}2\bar{1}0]$ in G1, which is consistent with the type determined by the EBSD-based misorientation analysis method (see Figure 2). In G2, the major dislocation slip is prismatic ⟨a⟩, which is consistent with the type determined by the conventional slip trace analysis (see Figure 1(a)).

The basal dislocation activities of other ten grains in this alloy were also revealed by the EBSD-based lattice rotation analysis. To further validate the present method, the slip systems determined by lattice rotation axis analysis have been compared to the slip line traces. The results are consistent. An example is included in Appendix A. It has to be noted the positioning for the starting point and the end point of the stretched (0001) pole (*e.g.*, points 1 and 2 in Figure 2(c)) will, to some extent, change the rotation axis determined by the present approach. For example, the variation angle about the averaged rotation axis is in the range of ± 5 deg. However, this uncertainty in angle is much smaller than the angles between the rotation axes of basal dislocation slip, 60 deg. It will not reduce the certainty for determining the subsurface basal slip type. However, it should be mentioned that this EBSD method for determination of dislocation slip is based on the same lattice rotation analysis approach which was originally developed for X-ray diffraction analysis of dislocation slip behavior of zirconium (Zr) single crystals.[30] Such an approach was later applied by Chun *et al.* for statistical analysis of in-grain misorientation axis (IGMA) based on EBSD images to determine the active slip modes in cold-rolled pure titanium (Ti) samples.[26] The difference between the present approach and the IGMA method is that their application fields are different. Due to the limited angular resolution of EBSD, even for the fully annealed Ti sample, 95 pct of the misorientation angles of neighboring scanning-grid pairs were found to be in the range of 0.5 to 0.97 deg.[26] So the lower cutoff misorientation angle included in IGMA analysis was taken as 1.2 deg. Accordingly, the lowest density of GND necessary to be detected by IGMA method can be roughly estimated by using the equation $\rho = \theta/b\delta$, where ρ is dislocation density, θ misorientation angle within a distance of δ, and b magnitude of Burgers vector.[31] With the 1.2 deg cutoff

Subsurface GND Distribution Map

G1

- □ light blue $(0001)[\bar{1}2\bar{1}0]$, 0.220
- □ magenta $(\bar{1}011)[\bar{1}2\bar{1}0]$, 0.481
- □ blue $(1\bar{1}01)[\bar{1}2\bar{1}3]$, 0.468
- □ green $(\bar{1}101)[\bar{1}2\bar{1}3]$, 0.213

G2
- □ red $(01\bar{1}0)[2\bar{1}\bar{1}0]$, 0.477
- □ orange $(01\bar{1}1)[2\bar{1}\bar{1}0]$, 0.394

□ Voxels without obvious stretched peaks

30 um
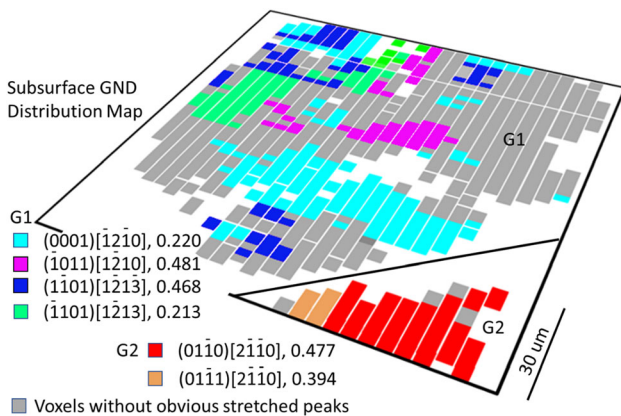
Fig. 4—GND distribution map of G1 and G2 based on the Laue diffraction peak streak analysis.

angle and the step size of EBSD scanning (0.5 μm in Reference 26), it can be calculated that only when the local density of GND is larger than 1.3×10^{14} m^{-2}, the dislocation slip can be distinguished. It means that IGMA method is only valid for metals subjected to high deformation strains or even severe plastic deformations. In contrast, the present method is based on the asterism of {0001} poles which provides the long-range lattice rotation information of local regions in grains and is less sensitive to the dislocation density. It is therefore able to reveal the dislocation activity of samples subjected to low deformation strains. Moreover, the specific Burgers vector of the activated basal $\langle a \rangle$ dislocation can be identified. Thus it can be considered as a complementary to the IGMA method as well. Application of such a method can be expected to bring deeper insights into the basal $\langle a \rangle$ dislocation behavior and the mechanisms related to basal $\langle a \rangle$ dislocations in Mg alloys.

In conclusion, the *subsurface* dislocation behavior of a deformed Mg-Y alloy was studied. One main achievement in this study is that a method based on local lattice rotation analysis using EBSD was proposed to identify the Burgers vector of basal $\langle a \rangle$ dislocations, especially for those not showing slip traces at grain surface. Its validity has been confirmed by the Laue diffraction technique. This method can serve as a complementary method to the conventional slip trace analysis and the IGMA method to determine the real basal $\langle a \rangle$ slip directions in grains.

APPENDIX A

Figure A1 shows another grain, which shows clear slip traces. By analyzing the spreading of the (0001) pole (Figure A1(c)), the rotation axis of G4 is determined as $\sim [10\bar{1}0]$, which indicates that the basal $\langle a \rangle$ dislocation slip with Burgers vector $[\bar{1}2\bar{1}0]$ has dominated the grain's deformation. This is consistent with the slip traces which are aligned along the basal planes of the crystal. An advantage of the method proposed in this work is that it can also determine the Burger vector of the slip system, which is not possible by only slip trace analysis.
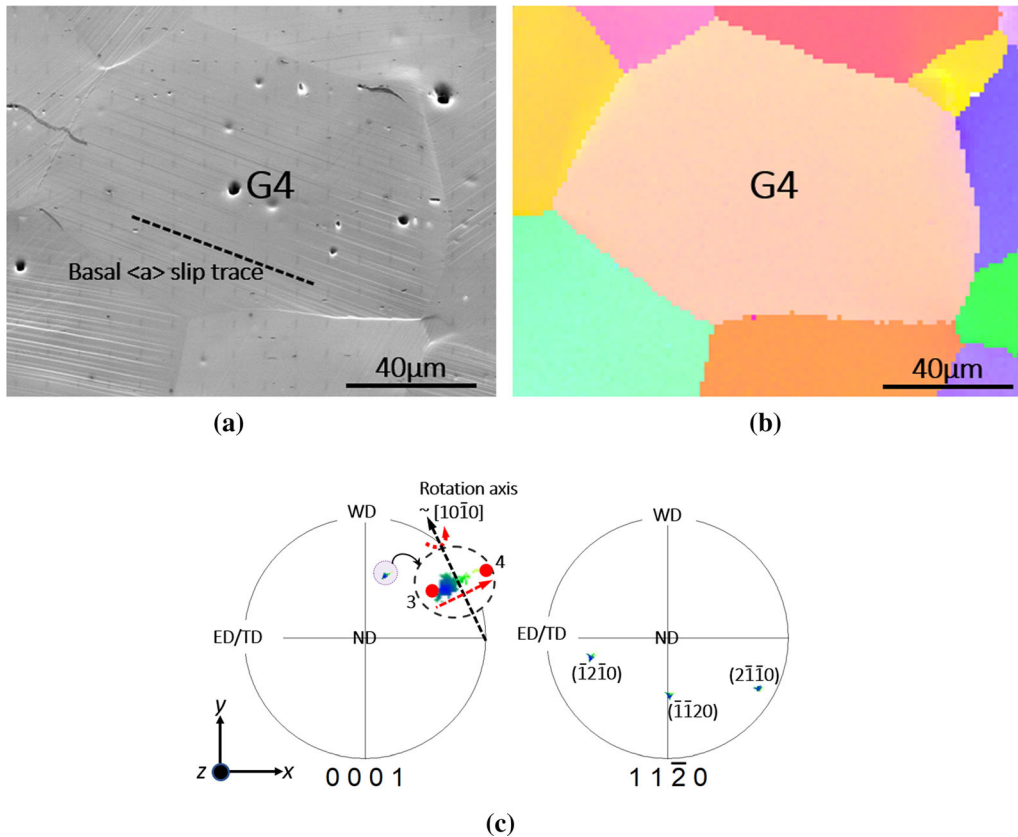
(a)

(b)

(c)

Fig. A1—EBSD-based lattice rotation analysis for another grain's basal dislocation activity. (*a*) SEM image of G4 and its neighboring grains. (*b*) Corresponding IPF map. (*c*) {0001} and {11$\bar{2}$0} pole figures of G4 where the (0001) pole is stretched nearly along the direction from the ($\bar{1}2\bar{1}0$) pole to the center of the {11$\bar{2}$0} pole figure. The rotation axis of G4 is ~ [10$\bar{1}$0].

REFERENCES

1. S. Sandlöbes, S. Zaefferer, I. Schestakow, S. Yi, and R. Gonzalez-Martinez: *Acta Mater.*, 2011, vol. 59, pp. 429–39.
2. K.H. Kim, J.B. Jeon, N.J. Kim, and B.J. Lee: *Scripta Mater.*, 2015, vol. 108, pp. 104–08.
3. K.H. Kim, J.H. Hwang, H.S. Jang, J.B. Jeon, N.J. Kim, and B.J. Lee: *Mater. Sci. Eng. A*, 2018, vol. 715, pp. 266–75.
4. S.R. Agnew, D.W. Brown, and C.N. Tomé: *Acta Mater.*, 2006, vol. 54, pp. 4841–52.
5. J. Sun, L. Jin, J. Dong, F. Wang, S. Dong, W. Ding, and A.A. Luo: *Int. J. Plast.*, 2019, vol. 123, pp. 121–32.
6. A. Khosravani, D.T. Fullwood, B.L. Adams, T.M. Rampton, M.P. Miles, and R.K. Mishra: *Acta Mater.*, 2015, vol. 100, pp. 202–14.
7. F. Wang, C.D. Barrett, R.J. McCabe, H. El Kadiri, L. Capolungo, and S.R. Agnew: *Acta Mater.*, 2019, vol. 165, pp. 471–85.
8. C.M. Cepeda-Jiménez, M. Castillo-Rodríguez, and M.T. Pérez-Prado: *Acta Mater.*, 2019, vol. 165, pp. 164–76.
9. C.M. Cepeda-Jiménez, J.M. Molina-Aldareguia, and M.T. Pérez-Prado: *Acta Mater.*, 2015, vol. 84, pp. 443–56.
10. D.F. Shi, M.T. Pérez-Pradoa, and C.M. Cepeda-Jiménez: *Acta Mater.*, 2019, vol. 180, pp. 218–30.
11. C.J. Boehlert, Z. Chen, I. Gutiérrez-Urrutia, J. Llorca, and M.T. Pérez-Prado: *Acta Mater.*, 2012, vol. 60, pp. 1889–1904.
12. C.J. Boehlert, Z. Chen, A. Chakkedath, I. Gutiérrez-Urrutia, J. Llorca, J. Bohlen, S. Yi, D. Letzig, and M.T. Pérez-Prado: *Philos. Mag.*, 2013, vol. 93, pp. 598–17.
13. H. Wang, C.J. Boehlert, Q.D. Wang, D.D. Yin, and W.J. Ding: *Int. J. Plast.*, 2016, vol. 84, pp. 255–76.
14. A. Chakkedath, J. Bohlen, S. Yi, D. Letzig, Z. Chen, and C.J. Boehlert: *Metall. Mater. Trans. A*, 2014, vol. 45A, pp. 3254–74.
15. B. Zhou, L. Wang, P. Jin, H. Jia, H.J. Roven, X. Zeng, and Y. Li: *Int. J. Plast.*, 2020, vol. 128, p. 102669.
16. X. Xu, D. Lunt, R. Thomas, R.P. Babu, A. Harte, M. Atkinson, J.Q. da Fonseca, and M. Preuss: *Acta Mater.*, 2019, vol. 175, pp. 376–93.
17. T.R. Bieler, P. Eisenlohr, C. Zhang, H.J. Phukan, and M.A. Crimp: *Curr. Opin. Solid State Mater.*, 2014, vol. 18, pp. 212–26.
18. T.R. Bieler, R. Alizadeh, M. Peña-Ortega, and J. Llorca: *Int. J. Plast.*, 2019, vol. 118, pp. 269–90.
19. Z. Huang, L. Wang, B. Zhou, T. Fischer, S. Yi, and X. Zeng: *Scripta Mater.*, 2018, vol. 143, pp. 44–48.
20. B.C. Larson, W.G. Yang, G.E. Ice, J.D. Budai, and J.Z. Tischler: *Nature*, 2002, vol. 415, pp. 887–90.
21. G.E. Ice and J.W. Pang: *Mater. Charact.*, 2009, vol. 60, pp. 1191–1201.
22. W.J. Liu, G.E. Ice, B.C. Larson, W.G. Yang, J.Z. Tischler, and J.D. Budai: *Metall. Mater. Trans. A*, 2004, vol. 35A, pp. 1963–67.
23. B. Zhou, L. Wang, W. Liu, J. Wang, X. Zeng, and W. Ding: *Mater. Charact.*, 2019, vol. 156, p. 109873.
24. H. Jia, K. Marthinsen, and Y. Li: *J. Alloys Comput.*, 2019, vol. 783, pp. 513–23.
25. S. Jin, K. Marthinsen, and Y. Li: *Acta Mater.*, 2016, vol. 120, pp. 403–14.
26. Y.B. Chun, M. Battaini, C.H.J. Davies, and S.K. Hwang: *Metall. Mater. Trans. A*, 2010, vol. 41A, pp. 3473–87.
27. T. Mayama, K. Aizawa, Y. Tadano, and M. Kuroda: *Comput. Mater. Sci.*, 2009, vol. 47, pp. 448–55.

28. R. Barabash, G.E. Ice, B.C. Larson, G.M. Pharr, K.-S. Chung, and W. Yang: *Appl. Phys. Lett.*, 2001, vol. 79, pp. 749–51.
29. C. Zhang, S. Balachandran, P. Eisenlohr, M.A. Crimp, C. Boehlert, R. Xu, and T.R. Bieler: *Scripta Mater.*, 2018, vol. 144, pp. 74–77.
30. E.J. Rapperport and C.S. Hartley: *Trans. Metall. Soc. AIME*, 1960, vol. 218, pp. 869–77.
31. H. Jia, R. Bjørge, L. Cao, H. Song, K. Marthinsen, and Y. Li: *Acta Mater.*, 2018, vol. 155, pp. 199–213.